Electron-lattice instabilities suppress cuprate-like electronic structures in $SrFeO_3/SrTiO_3$ superlattices

James M. Rondinelli* and Nicola A. Spaldin
Materials Department, University of California, Santa Barbara, California 93106-5050, USA
(Received 12 January 2010; published 10 February 2010)

Using *ab initio* density-functional theory we explore the behavior of thin layers of metallic d^4 $SrFeO_3$ confined between the d^0 dielectric $SrTiO_3$ in a superlattice geometry. We find that the presence of insulating $SrTiO_3$ spacer layers strongly affects the electronic properties of $SrFeO_3$: for single $SrFeO_3$ layers constrained to their bulk cubic structure, the Fermi surface is two dimensional, nested, and resembles that of the hole-doped superconducting cuprates. A Jahn-Teller instability couples to an octahedral tilt mode, however, to remove this degeneracy resulting in insulating superlattices.

DOI: 10.1103/PhysRevB.81.085109 PACS number(s): 74.78.Fk, 71.15.Mb, 71.30.+h, 74.72.−h

I. INTRODUCTION

Progress in the layer-by-layer growth of transition-metal oxide thin films[1,2] motivated the intriguing recent suggestion that oxide heterostructures engineered to have band structures close to those of the high-T_c cuprates could yield new superconductors.[3] Strained $LaNiO_3$ layers separated by inert spacers such as $LaAlO_3$ or $LaGaO_3$ were proposed as a promising trial system, with strain lifting the degeneracy of the single Ni^{3+} e_g electron and layering providing quasi-two-dimensionality. Indeed, first-principles electronic structure calculations[4] on Ni-based perovskite oxide superlattices constrained to their high-symmetry structure have found that, with careful choice of strain and local-interface chemistry,[5] two-dimensional (2D) Fermi surfaces resembling those of the hole-doped cuprates[6] can be obtained. Experimentally these superlattices, however, show neither high-temperature normal-state metallic resistivity nor low-temperature superconductivity possibly because competing electronic or structural instabilities are enhanced by epitaxial strain[7,8] and/or reduced dimensionality. Although high-T_c superconductivity tends to occur in materials with large electronic fluctuations and in close proximity to electronic, structural, or magnetic phase transitions,[9–12] strong electron-lattice coupling can also drive undesirable symmetry changes that are detrimental to the superconducting state.[13–16]

With these factors in mind, we examine how structural confinement and intrinsic lattice instabilities modify the electronic structure of $SrFeO_3$ in $SrTiO_3/SrFeO_3$ superlattices. Our motivation for this choice of system is threefold. First, like Ni^{3+}, Fe^{4+} has a single degenerate e_g electron in an octahedral environment that dictates its low-energy physics. The restriction on Fe-based compounds—traditionally dismissed from consideration for superconductivity because of their robust magnetism—has been lifted due to the recent discovery of superconducting Fe pnictides.[17] Second, bulk $SrFeO_3$ is metallic with *p*-type conductivity (like the doped cuprates) and is proximal to multiple instabilities: it manifests a long-wavelength spin-density wave, but neither Jahn-Teller distorts nor charge orders, even though both possibilities are suggested by its chemistry. Finally, unlike the structurally inert $LaAlO_3$ in the nickelate superlattices, $SrTiO_3$ is a highly polarizable dielectric, which can couple to electronic or structural distortions[18] in the $SrFeO_3$ layer.

Using first-principles density-functional theory (DFT) within the local-spin-density approximation (LSDA) plus Hubbard U (LSDA+U) method, we calculate the structure and electronic properties of $(SrTiO_3)_n/(SrFeO_3)_m$ superlattices. We focus on (i) the evolution of the 2D band structure with thickness of the dielectric and metal ($n,m=1$ or 3) and (ii) how competing structural and electronic instabilities manifest in the superlattices. We find that the 2D confinement from the superlattice periodicity along the growth (z) direction yields low-energy physics that are primarily derived from hybridized Fe $d_{x^2-y^2}$ and O $2p$ orbitals. The idealized high-symmetry superlattice structure has a strongly nested 2D Fermi surface that is similar to that of the parent superconductor La_2CuO_4.[19] Strong electron-lattice instabilities, enhanced by the 2D confinement, transform the metastable metallic structure into a lower-symmetry *insulating* superlattice.

II. COMPUTATIONAL DETAILS

Our LSDA+U DFT calculations are performed using the Vienna *ab initio* simulation package (VASP).[20,21] We follow the approach of Dudarev *et al.*[22] and include an effective Hubbard term $U_{\text{eff}}=U-J$ of 6 eV to treat the Fe $3d$ orbitals. This method and value of U_{eff} gave good results in earlier first-principles calculations for bulk $SrFeO_3$ and related iron oxide compounds.[23,24] The core and valence electrons are treated with the projector augmented wave method[25] with the following valence electron configurations: $3s^23p^64s^2$ (Sr), $3p^63d^74s^1$ (Fe), $3s^23p^63d^24s^2$ (Ti), and $2s^22p^4$ (O). The Brillouin-zone (BZ) integrations are performed with a Gaussian smearing of 0.05 eV over a $9\times9\times5$ Monkhorst-Pack k-point mesh[26] centered at Γ and a 450 eV plane-wave cutoff. For structural relaxations, we relax the ions until the Hellmann-Feynman forces are less than 1 meV $Å^{-1}$.

We construct the superlattices by stacking five-atom perovskite units along the z direction [see Fig. 1(d)] and constrain the in-plane lattice parameter (xy plane) to that of cubic local-density approximation (LDA) $SrTiO_3$ ($a=3.86$ Å) to simulate growth on a $SrTiO_3$ substrate. While the lattice mismatch between $SrFeO_3$ and $SrTiO_3$ is small (the theoret-

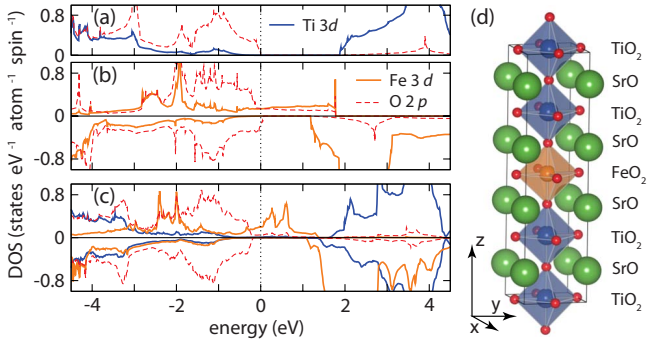

FIG. 1. (Color online) The DOS for (a) cubic $SrTiO_3$ (a=3.86 Å), (b) cubic FM $SrFeO_3$ (a=3.79 Å), and (c) the high-symmetry $P4/mmm$ $(SrTiO_3)_3/(SrFeO_3)_1$ superlattice shown in (d).

ical mismatch is 1.8%, with ferromagnetic (FM) LSDA+U $SrFeO_3$ having a=3.79 Å), we show below that it is sufficient to impose an epitaxial crystal field (Δ_{ECF}) that lifts the Fe e_g orbital degeneracy. We then relax the length of the c axis and the internal degrees of freedom along the z direction. The in-plane periodicity imposed by this choice of reference structure does not permit cell-doubling structural distortions such as octahedral rotations or orbital ordering: this highly symmetric superlattice mimics the structural constraints often considered to be imposed in heteroepitaxial thin films. We relax this restriction later to study electron-driven lattice instabilities.

FM order is imposed on the Fe sites in all calculations and is theoretically[24] found to be the lowest-energy collinear ordering for bulk $SrFeO_3$. The experimentally observed antiferromagnetism results from a long-wavelength screw structure in which the angle between neighboring spins rotates by ~40° along the [111] direction[27] due to strong ferromagnetic nearest-neighbor interactions.

III. RESULTS AND DISCUSSION

A. Electronic structure of the ideal superlattice

We begin by studying the electronic structure of the high-symmetry $(SrTiO_3)_3/(SrFeO_3)_1$ superlattice (Table I). We plot in Fig. 1 our calculated local densities of states (DOSs) for cubic $SrTiO_3$ [Fig. 1(a)], cubic $SrFeO_3$ [Fig. 1(b)], and the superlattice [Fig. 1(c)]. Our results for the bulk compounds are consistent with the literature: in $SrTiO_3$ we obtain a ~2 eV band gap between an O $2p$ valence band and a Ti $3d$ conduction band. $SrFeO_3$ is nearly half-metallic with a calculated magnetic moment of $3.8\mu_B$ per Fe atom, consistent with a high-spin d^4 electronic configuration. The Fermi level (dashed line at 0 eV) lies in a region of majority-spin Fe $e_g^{\uparrow}$-O $2p^{\uparrow}$ hybridized orbitals and in the O $2p^{\downarrow}$ valence band. The electronic structure of the superlattice is close to a superposition of its constituents, except for a reduction in the contribution of the O $2p$ states at E_F making the superlattice half-metallic. While the use of the Hubbard U method in DFT calculations is known to drive bands toward integer filling, the half-metallicity is robust for U=0–8 eV. The FM order, as in the bulk, is the lowest-energy collinear spin configuration, with the checkerboard 97 meV and the striped antiferromagnetic order 45 meV per five-atom unit cell higher in energy.

TABLE I. Calculated structural data used in this work for the reference $(SrTiO_3)_3/(SrFeO_3)_1$ superlattice. The in-plane lattice constant is constrained to the optimized LDA value for $SrTiO_3$, and the c axis is also optimized: the lattice parameters are $a=b$ =3.86 Å and c=15.241 Å in space group $P4/mmm$.

Atom	Wyckoff	x	y	z
Sr_1	$2h$	$\frac{1}{2}$	$\frac{1}{2}$	0.126
Sr_2	$2h$	$\frac{1}{2}$	$\frac{1}{2}$	0.622
Ti_1	$2g$	0	0	0.252
Ti_2	$1a$	0	0	0
Fe_1	$1b$	0	0	$\frac{1}{2}$
O_1	$4i$	0	$\frac{1}{2}$	0.252
O_2	$2f$	0	$\frac{1}{2}$	0
O_3	$2e$	0	$\frac{1}{2}$	$\frac{1}{2}$
O_4	$2g$	0	0	0.126
O_5	$2g$	0	0	0.622

We plot the band structure of the $P4/mmm$ superlattice in Figs. 2(a) and 2(b) using the "fat-band" method[28] in which the magnitude of the projection of each Bloch state onto a particular set of atomic orbitals is represented by its linewidth: Fig. 2(a) shows the equatorial O $2p_{x,y}$-Fe $3d_{x^2-y^2}$ states and Fig. 2(b) shows the O $2p_z$-Fe $3d_{z^2}$ orbitals. Consistent with the DOS, we find partial occupation of the majority $d_{x^2-y^2}$ and d_{z^2} Fe states at E_F with the energy of the $d_{x^2-y^2}$ at Γ 0.50 eV lower than that of the d_{z^2} orbital. The energy difference at Γ is explained from compression of the apical (1.88 Å) over the in-plane (1.93 Å) Fe-O bond

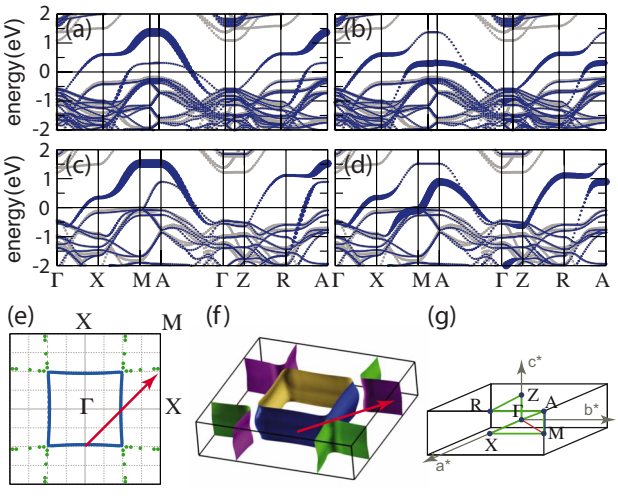

FIG. 2. (Color online) Electronic band-structure plots for the [(a) and (b)] n=3, m=1 and [(c) and (d)] n=1, m=1 superlattices. (a) and (c) show the majority-spin fat bands (blue, heavy lines) derived from O $2p_{x,y}$-Fe $3d_{x^2-y^2}$ states, whereas (b) and (d) show the O $2p_z$-Fe $3d_{z^2}$ states. The Fermi surface at (e) k_z=0 and in the full (f) BZ shown in (g) consists of two bands connected by the $\mathbf{Q}=(1,1,0)\frac{\pi}{a}$ interband nesting vector (arrow).

length from the imposed Δ_{ECF}.[4] Interestingly, the apical Fe-O distance is shorter than the value (1.90 Å) that we obtain when we force *bulk* $SrFeO_3$ to have the $SrTiO_3$ in-plane lattice constant, suggestive of an additional spontaneous Jahn-Teller-like distortion (we examine this later). Despite the substrate elongation of the equatorial Fe-O bonds, the bands of $d_{x^2-y^2}$ character do not fully split from the d_{z^2} bands to produce a single band crossing E_F; in fact, both the top and the bottom of the e_g band are dominated by $d_{x^2-y^2}$ states. The d_{z^2} band can likely be further destabilized to achieve an identical cuprate-like electronic structure with additional strain[3] and/or chemical modifications.[4]

We now investigate the character of the 2D bands and examine how the electronic structure at E_F responds to changes in the dielectric thickness by comparing the full band structures of the $(SrTiO_3)_3/(SrFeO_3)_1$ [Figs. 2(a) and 2(b)] and $(SrTiO_3)_1/(SrFeO_3)_1$ [Figs. 2(c) and 2(d)] superlattices. As expected, the bandwidth of the $d_{x^2-y^2}$ derived states along Γ-A is nearly the same in the two superlattices due to identical in-plane structural parameters. The dispersion of the d_{z^2} bands is markedly different, however, with the less confined $n=1$, $m=1$ superlattice having a larger bandwidth than the more confined $n=3$, $m=1$ along the M-A lines. Increasing dielectric thickness ($n=1,\ldots,4$) shows that the dispersive $d_{x^2-y^2}$ bands saturate at ~ 2 eV in width while the d_{z^2} states are almost dispersionless, although never fully split. In contrast, increasing the thickness of the $SrFeO_3$ layers in the superlattice produces several partially occupied e_g bands crossing E_F, and the band structure (not shown) resembles a regular metal. We conclude that a cuprate-like band structure is unlikely in superlattices containing multiple ferrate layers.

The 2D confinement is discernible in the Fermi surface of the $n=3$, $m=1$ superlattice shown in Figs. 2(e) and 2(f). The additional band crossing E_F in the $k_z=0$ plane, not seen in the $n=1$, $m=1$ [Figs. 2(c) and 2(d)] superlattice nor bulk $SrFeO_3$ lattice matched to $SrTiO_3$, produces squared-cylindrical arrays around the M point consistent with the fourfold symmetry of the lattice. An unusual inward bowing along the Γ-X direction occurs with corrugations along k_z similar to overdoped cuprates. The band curvature indicates electron and hole sheets at Γ and M, respectively, similar in character to the superconducting cuprates.[19,29] Interestingly, the two Fermi sheets nearly intersect at half the Γ-M distance producing a nesting vector $\mathbf{Q}=(1,1,0)\frac{\pi}{a}$ connecting them. Such a vector can result in a charge- or spin-density wave, or for strong coupling of the electronic system to the lattice, a symmetry lowering structural distortion. These two sheets are largely insensitive to the calculation details: changing U weakly affects the band crossings at E_F since the electronic structure is mainly modified by the confining $SrTiO_3$ layers. Spin-orbit interactions also do not alter the FS nesting.

B. Competing lattice instabilities

We now investigate possible structural instabilities in the $(SrTiO_3)_3/(SrFeO_3)_1$ superlattice, and their influence on the FS degeneracy. We identify likely structural distortions that connect the high-symmetry reference phase to low-symmetry structures by atomic displacements that maintain a direct group-subgroup relation. These structural distortions or modes are associated with different irreducible representations (irreps) of the parent space group, and the contribution of each mode in the distorted structure can be decomposed using a symmetry-mode analysis.[30,31] The advantage of the technique is that it allows a complicated structural distortion to be reduced to a unique set of symmetry modes of the parent phase from which local atomic displacement vectors can be found.

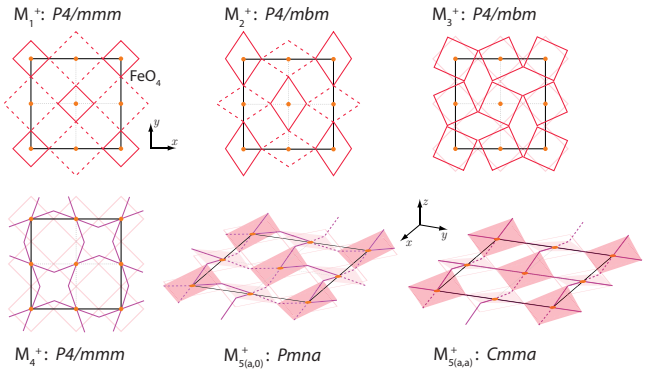

FIG. 3. (Color online) Illustrations of the structural distortions that may couple with the electronic system: M_1^+ breathing mode, M_2^+ stretch mode, M_3^+ rotation mode of the FeO_6 octahedra around the z direction, M_4^+ bending of the Fe-O bonds (purple, solid lines), and two different tilt patterns $M_5^+(a,0)$ and $M_5^+(a,a)$ in the xy plane.

We identify the symmetry breaking distortions of the reference ($n=3$, $m=1$) superlattice in space group $P4/mmm$ by choosing those that are commensurate with the nesting vector $\mathbf{Q}$. Irreps of the same wave vector as the symmetry degeneracy occur at the zone edge $k=(\frac{1}{2},\frac{1}{2},0)$ and following the conventions of Miller and Love are denoted as M_i^+ (with $i=1,\ldots,5$). Although there are five additional irreps labeled M_i^- for the space group $P4/mmm$, we do not consider them since they have antisymmetric distortions with respect to the inversion operator. Our fully relaxed *ab initio* structures are then reduced into combinations of these irreps by performing a symmetry-mode analysis[30] that makes accessible the local atomic displacements. We keep FM spin order fixed through the analysis to isolate the electron-lattice coupling.

The active irreps we examine (Fig. 3) affect either the equatorial Fe-O bond lengths (crystal field) or O-Fe-O bond angles ($dp\sigma$ bandwidth). Irreps M_1^+ and M_2^+ are planar breathing and stretch modes of the FeO_4 plaquettes, respectively, and are anticipated to strongly modulate the $e_g^{\uparrow}$-O $2p$ hybridization at E_F. The M_1^+ mode produces two unique FeO_4 plaquettes arranged in a 2D checkerboard manner and gives rise to charge disproportionation in bulk isoelectronic $CaFeO_3$.[32] In contrast the M_2^+ irrep, or Jahn-Teller mode, creates two long and two short equatorial Fe-O bonds and favors orbital polarization. The remaining irreps are collective distortions of the octahedral units that produce the common tilt and rotation patterns found in perovskite oxides. These modes affect the $dp\sigma$ bandwidth through deviations in the Fe-O-Fe bond angle away from the ideal 180°: M_3^+ consists of rotations of the in-plane oxygen atoms about the z axis; M_4^+ produces a bending distortion of the O-F-O bond; and the

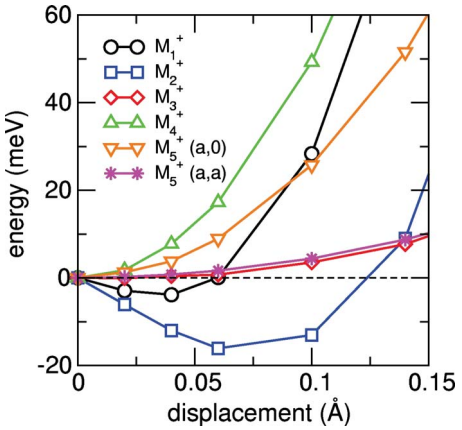

FIG. 4. (Color online) Evolution of the total energy (per five-atom perovskite cell) for irreps M_i^+ (with $i=1,\ldots,5$) frozen into the $SrFeO_3$ layer of the $(SrTiO_3)_3/(SrFeO_3)_1$ superlattice relative to the high-symmetry structure given in Table I.

2D irrep M_5^+ produces two possible tilt patterns of the planar oxygen atoms: $M_5^+(a,0)$ giving a pattern with space group symmetry *Pmna* or $M_5^+(a,a)$ with *Cmma*.

C. Electron-lattice coupling and energetics

We begin the analysis of the effect of the M-point irreps on the electronic structure of the $n=3$, $m=1$ superlattice by first "freezing" each irrep as a function of mode amplitude into the equatorial oxygen atoms coordinating each Fe atom. (For each irrep we increase the size of superlattice to be commensurate with the atomic distortion pattern.) At the same time, we keep the remaining atoms in the superlattice clamped to the reference $P4/mmm$ positions to isolate the response of the ferrate layer—displacements of other atoms in the superlattice are obtained later through full structural optimization.

We first evaluate how the total energy changes as a function of each mode amplitude. This is done by performing total-energy calculations at a fixed displacement magnitude of equatorial oxygen atoms about the Fe atoms. The change in total energy is shown in Fig. 4 for each irrep normalized to a five-atom perovskite unit cell. It is clear that the two modes which affect the Fe-O bond length, M_1^+ and M_2^+, both lower the energy of the superlattice. The sensitivity of the total energy on the Fe-O bond length is not too surprising in this case since the states near the Fermi level in the superlattice are derived from the Fe $e_g^\uparrow$ orbitals which point directly at the O $2p$ orbitals; therefore, any direct changes to the bonding $e_g^\uparrow$-O $2p$ orbital overlap via a structural distortion lowers the total energy through chemical bond formation. In addition, the rotational mode M_3^+ lowers the energy: although most octahedral instabilities require long-range cooperation, the M_3^+ mode is effectively decoupled from one layer to the next, and therefore does not require coherency of the oxygen octahedra to be energy lowering. In contrast, the other octahedral tilt instabilities all raise the energy of the system: this can be understood from the fact these irreps require a collective motion of all oxygen octahedra, and not just those in the ferrate layer.

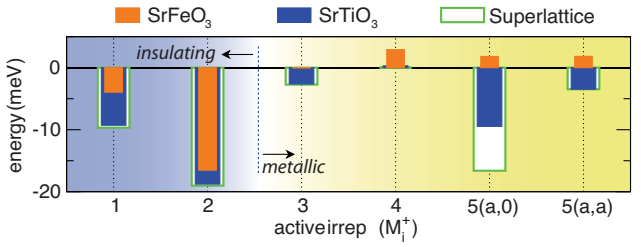

FIG. 5. (Color online) Electronic responses from $SrFeO_3$ (orange, light bars), $SrTiO_3$ (blue, dark bars), and the full superlattice (green, empty bars) to the M_i^+ irreps.

The energy change due to the optimal mode amplitude for each irrep frozen in the ferrate layer is shown in Fig. 5 with respect to the high-symmetry $P4/mmm$ superlattice (energies per five-atom perovskite cell). For irreps which raise the energy of the superlattice, we take a displacement value of 0.05 Å for comparison. We find that irreps M_1^+, M_2^+, and M_3^+ lower the energy of the *superlattice*. In contrast they increase the energy of bulk $SrFeO_3$ lattice matched to $SrTiO_3$, indicating that the superlattice geometry and the e_g orbital degeneracy are more susceptible to structural distortions. The remaining irreps which require collective cooperation of all oxygen octahedra increase the superlattice energy when the dielectric is clamped to the reference configuration.

Next, we fully relax the $SrTiO_3$ with the ferrate atoms fixed to the distortions above within the symmetry constraints imposed by each irrep to isolate the effect of the dielectric response. Now every irrep except M_4^+ is found to be energy lowering: the large energy gain now observed for the M_5^+ modes suggests that a three-dimensional tilt pattern is preferred—this result is likely driven by the fact that most of the superlattice is $SrTiO_3$, which itself has a large M_5^+-like mode instability.

We now relax both constituents under the symmetry constraints imposed by the irreps to find the lowest-energy atomic configurations. The largest energy-lowering distortions are found to be the Jahn-Teller and tilt modes, both of which are more favorable than the breathing distortion that also directly modifies the e_g states at the Fermi level. The breathing mode (M_1^+) produces two FeO_6 octahedra which differ in volume by 8.1% due to the different equatorial bond lengths of 1.96 and 1.90 Å. In contrast, the stretch mode (M_2^+) produces planar Fe-O bonds of 2.01 and 1.86 Å, with an octahedral volume less than 0.40% different from the reference structure.

Both irreps M_1^+ and M_2^+ open energy gaps at the Fermi level in the superlattice [Figs. 6(b) and 6(c)], while identical distortions in bulk $SrFeO_3$ maintain its metallicity. The tilt modes $M_5^+(a,0)$ and $M_5^+(a,a)$ are more unstable than the rotation M_3^+ irrep, with $M_5^+(a,0)$ almost as energetically favorable as the Jahn-Teller distortion. In the single tilt mode $M_5^+(a,0)$, the Fe-O-Fe in-plane bond angle is reduced from the bulk 180° by 5.7°, and the out-of-plane interfacial Fe-O-Ti bond angle is also reduced by 8.6°. Yet, due to the weaker influence of the bond angle on the $dp\sigma$ bandwidth, none of the bond angle distortions gap the FS. There is a 0.24 eV bandwidth reduction, however, for irrep M_5^+ shown in Fig. 6(d). Similarly, the M_1^+ mode also gaps the Fermi

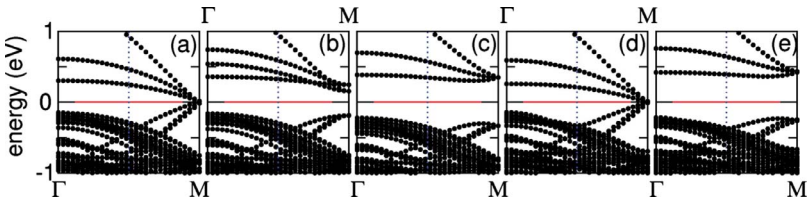

FIG. 6. (Color online) Band structure for (a) the $P4/mmm$ ($n=3$, $m=1$) superlattice as in Fig. 2(a) with the lattice parameter doubled in plane to allow comparison with (b)–(d) which include additional structural distortions, (b) M_1^+, (c) M_2^+, and (d) $M_5^+(a,0)$, and (e) the ground-state $P2_1/c$ structure.

surface—although it is not an energy-lowering distortion—in doped La_2CuO_4, whereas the octahedra tilt and rotation modes, which are found in the cuprates, show minor effects on the electronic structure.[33]

D. Metal-insulator transition

We next calculate the fully optimized structure starting from a combination of the M_2^+ and M_5^+ irreps and examine the change in the electronic structure of the $(SrTiO_3)_3/(SrFeO_3)_1$ superlattice. Our ground-state structure is 33.5 meV lower in energy (per five-atom unit cell) than the reference superlattice. It contains FeO_4 plaquettes with bond lengths of 1.86 and 2.01 Å due to the Jahn-Teller mode that makes the superlattice insulating [0.58 eV gap, Fig. 6(e)], while also enhancing the ferromagnetic superexchange[34,35] among the degenerate orbitals; an antiferromagnetic checkerboard arrangement, for example, is 50 meV higher in energy. The octahedral instabilities largely condense in the $SrTiO_3$ layers with reduced interaction in the ferrate plane: the in-plane Fe-O-Fe bond angle is reduced by 6.89° while a 10° reduction occurs across the Fe-O-Ti angle. By symmetry decomposing the structure (Table II) as a combination of the $P4/mmm$ irreps, $0.051\Gamma_1^+ + 0.048\Gamma_5^+ + 0.21M_2^+ + 0.13M_3^+ + 0.97M_5^+$, we find that the primary order parameters M_2^+ and M_5^+ drive the $P4/mmm$ $(a^0,a^0,c^0) \rightarrow P2_1/c$ (a^-,a^-,c^+) metal-insulator transition, with the associated change in octahedral tilt patterns. After this distortion, the Γ_5^+ and M_3^+ components are allowed to be nonzero without further symmetry reduction, thus making them secondary order parameters. Since none of these distortions are favored in bulk $SrFeO_3$, we attribute the electron-lattice coupling enhancement to the confinement effects imposed by the superlattice geometry.

IV. CONCLUSION

We have demonstrated that, in a superlattice geometry, confinement from dielectric spacer layers combines with a strain-induced epitaxial crystal field (Δ_{ECF}) to modify the energies and dispersions of apical d_{z^2} and in-plane Fe $d_{x^2-y^2}$ orbitals. When we simulate superlattices with the high-symmetry cubic structures adopted by room-temperature $SrTiO_3$ and $SrFeO_3$, partial planar electron localization yields a 2D Fermi surface that resembles that of the superconducting cuprates. Low-energy M-point instabilities compete with nesting on the Fermi surface to make the superlattices proximal to multiple competing phases. The lattice instabilities are enhanced by the dielectric $SrTiO_3$ layers; therefore, inert spacer layers without polarizable ions might be more favorable for superconductivity. We hope that our finding of competing structural ground states with distinct electronic properties motivates experimental investigation of $SrFeO_3/SrTiO_3$ heterostructures using external electric and magnetic fields: such probes could tune between the itinerant

TABLE II. Different lattice instabilities that reduce the $P4/mmm$ ($n=3,m=1$) superlattice to the ground-state structure $P2_1/c$. The isotropy subgroups, normalized displacement vectors, and amplitudes are given for each irrep present in the ground-state structure. We provide the common molecular spectroscopy labels for each atom, and note that all atoms in irrep Γ_1^+ are given the symmetry A_1 as listed after the last atom in that distortion.

Irrep	Space group	Dimension	Normalized amplitude	Normalized displacement vector	Amplitude (Å)
Γ_1^+	123 $P4/mmm$	(a)	0.051	0.32 Sr_1 −0.74 Sr_2 +0.034 Ti_1 −0.58 O_1 +0.12 O_4 −0.017 $O_5(A_1)$	0.036
Γ_5^+	12 $C2/m$	(a)	0.048	0.051 $Sr_1(E)$ −0.52 $Sr_2(E)$ +0.23 $Ti_1(E)$ −0.38 $O_1(B_2)$ +0.51 $O_2(B_1)$ +0.24 $O_4(E)$ −0.46 $O_5(E)$	0.034
M_2^+	127 $P4/mbm$	(a)	0.21	−0.025 $O_1(B_2)$ +0.99 $O_3(B_{2u})$	0.15
M_3^+	127 $P4/mbm$	(a)	0.13	−0.91 $O_1(B_1)$ +0.40 $O_2(B_{3u})$	0.090
M_5^+	53 $Pmna$	$(a,0)$	0.97	−0.012 $Sr_1(E)$ +0.13 $Ti_1(E)$ −0.49 $O_1(A_1)$ +0.38 $O_2(B_{1u})$ +0.34 $O_3(B_{1u})$ +0.52 $O_4(E)$ +0.48 $O_5(E)$	0.68

and localized electronic states in analogy with the parent Mott insulating cuprates.

ACKNOWLEDGMENTS

We gratefully acknowledge support from NDSEG (J.M.R.) and the NSF under Grant No. DMR 0940420 (N.A.S.), and discussions with C. Adamo, D. Schlom, K. Delaney, O. K. Andersen, and W. Pickett. Portions of this work made use of the SGI Altix COBALT system at the National Center for Supercomputing Applications under Grant No. TG-DMR-050002S, and the CNSI Computer Facilities at UC Santa Barbara under NSF Award No. CHE-0321368.

*Author to whom correspondence should be addressed; rondo@mrl.ucsb.edu

[1] H. Y. Hwang, Science **313**, 1895 (2006).
[2] J. W. Reiner, F. J. Walker, and C. H. Ahn, Science **323**, 1018 (2009).
[3] J. Chaloupka and G. Khaliullin, Phys. Rev. Lett. **100**, 016404 (2008).
[4] P. Hansmann, X. Yang, A. Toschi, G. Khaliullin, O. K. Andersen, and K. Held, Phys. Rev. Lett. **103**, 016401 (2009).
[5] O. Andersen, APS March Meeting, 2009 (unpublished); http://meetings.aps.org/link/BAPS.2009.MAR.Q30.4
[6] E. Pavarini, I. Dasgupta, T. Saha-Dasgupta, O. Jepsen, and O. K. Andersen, Phys. Rev. Lett. **87**, 047003 (2001).
[7] Y. Ogimoto, M. Nakamura, N. Takubo, H. Tamaru, M. Izumi, and K. Miyano, Phys. Rev. B **71**, 060403 (2005).
[8] J. Cao *et al.*, Nat. Nanotechnol. **4**, 732 (2009).
[9] E. Morosan, H. W. Zandbergen, B. S. Dennis, J. W. G. Bos, Y. Onose, T. Klimczuk, A. P. Ramirez, N. P. Ong, and R. J. Cava, Nat. Phys. **2**, 544 (2006).
[10] A. D. Bianchi *et al.*, Science **319**, 177 (2008).
[11] N. Nagaosa, Science **275**, 1078 (1997).
[12] C. de la Cruz *et al.*, Nature (London) **453**, 899 (2008).
[13] G. Bilbro and W. L. McMillan, Phys. Rev. B **14**, 1887 (1976).
[14] P. B. Allen, in *Dynamical Properties of Solids*, edited by G. K. Horton and A. A. Maradudin (North-Holland, New York, 1980), Vol. 3, pp. 95–196.
[15] J. D. Jorgensen, H. B. Schüttler, D. G. Hinks, D. W. Capone II, K. Zhang, M. B. Brodsky, and D. J. Scalapino, Phys. Rev. Lett. **58**, 1024 (1987).
[16] J. M. An, S. Y. Savrasov, H. Rosner, and W. E. Pickett, Phys. Rev. B **66**, 220502 (2002).
[17] Y. Kamihara, T. Watanabe, M. Hirano, and H. Hosono, J. Am. Chem. Soc. **130**, 3296 (2008).
[18] S. Okamoto, A. J. Millis, and N. A. Spaldin, Phys. Rev. Lett. **97**, 056802 (2006).
[19] R. E. Cohen, W. E. Pickett, L. L. Boyer, and H. Krakauer, Phys. Rev. Lett. **60**, 817 (1988).
[20] G. Kresse and J. Furthmüller, Phys. Rev. B **54**, 11169 (1996).
[21] G. Kresse and D. Joubert, Phys. Rev. B **59**, 1758 (1999).
[22] S. L. Dudarev, G. A. Botton, S. Y. Savrasov, C. J. Humphreys, and A. P. Sutton, Phys. Rev. B **57**, 1505 (1998).
[23] T. Saha-Dasgupta, Z. S. Popović, and S. Satpathy, Phys. Rev. B **72**, 045143 (2005).
[24] I. Shein, K. Shein, V. Kozhevnikov, and A. Ivanovskii, Phys. Solid State **47**, 2082 (2005).
[25] P. E. Blöchl, Phys. Rev. B **50**, 17953 (1994).
[26] H. J. Monkhorst and J. D. Pack, Phys. Rev. B **13**, 5188 (1976).
[27] T. Takeda, Y. Yamaguchi, and H. Watanabe, J. Phys. Soc. Jpn. **33**, 967 (1972).
[28] O. Jepsen and O. K. Andersen, Z. Phys. B: Condens. Matter **97**, 35 (1995).
[29] W. E. Pickett, R. E. Cohen, and H. Krakauer, Phys. Rev. B **42**, 8764 (1990).
[30] M. I. Aroyo, A. Kirov, C. Capillas, J. M. Perez-Mato, and H. Wondratschek, Acta Crystallogr., Sect. A: Found. Crystallogr. **A62**, 115 (2006).
[31] D. Orobengoa, C. Capillas, M. I. Aroyo, and J. M. Perez-Mato, J. Appl. Crystallogr. **42**, 820 (2009).
[32] J. Matsuno, T. Mizokawa, A. Fujimori, Y. Takeda, S. Kawasaki, and M. Takano, Phys. Rev. B **66**, 193103 (2002).
[33] L. F. Mattheiss, Phys. Rev. Lett. **58**, 1028 (1987).
[34] J. Goodenough, J. Phys. Chem. Solids **6**, 287 (1958).
[35] J. Kanamori, J. Phys. Chem. Solids **10**, 87 (1959).